ChemElectroChem

Research Article
doi.org/10.1002/celc.202300183

Chemistry Europe
European Chemical Societies Publishing

www.chemelectrochem.org

Deep Eutectic $Mn(NO_3)_2$—H_2O Binary System as a Safe, Cost-Effective, and Efficient Electrolyte for Supercapacitor Applications

Mohamed Raghibi,[a] Georgios Nikiforidis,[b] and Mériem Anouti*[a]

Deep eutectic solvents (DESs) have proved to be an effective substitute for conventional electrolytes for energy storage applications because of their unique properties and ability to adapt them to specific applications. In this regard, this study examines an easy-to-produce, widely available and cheap manganese nitrate concentrated electrolyte that holds DES traits. The electrolyte (i.e., manganese nitrate; $(Mn(NO_3)_2 \cdot 6H_2O$ with a weight composition of 42%) revealed its eutectic behaviour by benchmarking the eutectic distance (53 °C), thermal expansion coefficient (3.9×10^{-4} K), activation energy for conductivity (~2.45 kJ mol^{-1}), and viscosity (14 kJ mol^{-1}). What's more, it was successfully incorporated into a two-electrode symmetric supercapacitor comprising activated carbon electrodes and demonstrated specific capacitance retention of 93% (170 F g^{-1}) through 2000 consecutive galvanostatic charge-discharge cycles at 25 and −20 °C.

Introduction

Aqueous electrolytes are commonly used in electrochemical systems and processes due to their effectiveness and viability towards sustainability. Their ionic conductivity can stretch to values greater than 150 mS cm^{-1} (except for very low temperatures), markedly higher than non-aqueous electrolytes.[1] Besides, they are safe, non-flammable,[2] non-toxic, in several instances affordable[3] compared to their peers (i.e., organic solvents,[3] supercritical fluids,[4] room-temperature ionic liquids[5] and poly-fluorinated compounds[6]), widely available, and easy to synthesize. Yet, they are hindered by their thermal and electrochemical stability.[7] For example, in supercapacitors, conventional aqueous electrolytes (e.g., H_2SO_4, KCl, and KOH) are hindered by low voltage, which in turn limits their energy density.[8] Both hydrogen and oxygen evolution reactions require an overpotential that is contingent on the electrode material,[9] and when exceeded can propagate decomposition and instability within the medium and the electrode(s) (e.g., corrosion and leakage[10]), reducing the performance and lifespan of the device. Therefore, novel ways to improve their performance are actively researched and developed. It has been reported that the interaction between ions and solvents in electrolytes can mitigate the water decomposition process and the production of hydrogen gas, especially in concentrated aqueous solutions,[11] allowing for high-voltage operation and effectively competing with non-aqueous solutions.[12]

Another strategy to tackle the constraints of aqueous electrolytes entails the inception of new, environmentally friendly, and sustainable electrolytes. Deep eutectic solvents (DESs) fit those requirements.[13,14] They exhibit low toxicity and non-flammability and in doing so, are deemed suitable for industrial processes and electrochemical applications.[15] DESs commonly consist of a hydrogen-bond-accepting (HBA) component and a hydrogen-bond-donating (HBD) component at a specific molar ratio.[16] They are typically liquid at ambient conditions and comprise two components, with the freezing point of the DESs being much lower than the melting points of the two components.[17]

DESs can be aqueous-based; that is composed of ice and another component such as metal salts.[18] An early X-ray diffraction study[19] described a model with hydrated ions $M(H_2O)_n$-X (where M denotes Mn, Fe, Ce, Zn, Al and X represents SO_4^{2-} or NO_3^-) as independent components (in the thermodynamic sense) interacting with the outer shell of water molecules. This intriguing attribute gives rise to unconventional aqueous salt hydrates that can be introduced in a wide range of industrial applications, including advanced batteries based on Zn, Mg and Ca[20] and supercapacitors.[21] Mixtures of water and certain di- and trivalent metal salts in polyhydrated congruent state (i.e., $MX(H_2O)_n$ where M denotes Mn, Mg, Ca, Zn and X is the counter ion) form liquid eutectics at low temperatures and exhibit all the known properties of DESs when considering hydrated cations as independent entities. More specifically, the complex $M(H_2O)_n$ acts as the HBA (H-bond acceptor) component of the DES and water (ice) assumes the role of the HBD component.

In the search for unconventional aqueous salt hydrates, manganese nitrate ($Mn(NO_3)_2$) is a suitable candidate due to its

[a] M. Raghibi, Prof. M. Anouti
Laboratoire PCM2E
Université de Tours
Parc de Grandmont, 37200 Tours (France)
E-mail: meriem.anouti@univ-tours.fr
[b] Dr. G. Nikiforidis
Institute for Materials Discovery
University College London
Malet Place, London, WC1E 7JE (UK)

Supporting information for this article is available on the WWW under https://doi.org/10.1002/celc.202300183

high solubility in water, viz., up to 80% in weight of $Mn(NO_3)_2$ can be dissolved in water.[22] Manganese is abundant, inexpensive ($10 per kg) and has a low environmental load.[23] $Mn(NO_3)_2$ exhibits a complex behavior with four types of hydrated salt, viz., $Mn(NO_3)_2 \cdot n(H_2O)$ where *n* equals 1, 2, 4 and 6, and hence can form several aqueous-based DES mixtures.[24] The available physical and thermal experimental data are scarce for these mixtures. There are, however, reported theoretical models that compute the eutectic phase diagram by an extended UNIQUAC model[24].[25]

In the field of supercapacitors (SCs), manganese nitrate is mainly used in the design of electrodes and there is ongoing work to optimize its performance and overcome any limitations. For example, manganese nitrate (i.e., manganese nitrate hexahydrate ($Mn(NO_3)_2 \cdot 6H_2O$) and manganese nitrate monohydrate ($Mn(NO_3)_2 \cdot H_2O$)) have been widely used as precursors for the fabrication of a variety of supercapacitor electrode materials (e.g., MnO_2 nanotubes, microspheres, Mn-doped ZnS nanosheets, $CoMn_2O_4$ nanofibers)[26] in a cost-effective, simple and somewhat green manner. However, to our knowledge, no work has been reported on its use as an electrolyte.

To this end, predicated on the fact that 40% mass of $Mn(NO_3)_2$ in water (4 mol kg^{-1}) shows a DES character,[24] the physicochemical properties of four concentrated aqueous solutions of $Mn(NO_3)_2$, (considered as deep eutectic $Mn(NO_3)_2$-H_2O systems) are investigated in this study followed by their viability for rapid storage applications. The first part of this study is devoted to the physical characterization of these solutions followed by the discussion of their volumetric and transport properties (conductivity, viscosity, and ionicity) in relation to their structure at the molecular level. The second part is dedicated to the suitability of these solutions in symmetrical two-electrode supercapacitors comprising activated carbon (which holds a high specific surface area along with surface oxygenated species) in terms of thermal stability and cycleability.

Results and Discussion

Physical characterisation

While molten salt hydrates have a concentration limit (e.g., AX, nH_2O) close to that of aqueous solutions, their phase diagrams are identical to those of all DESs in the Abbott classification,[27] exhibiting in the eutectic region strong and dissociating HBD-HBA interactions. Before proceeding with the physical characterization of the investigated solutions (Table 1), their mass composition on the eutectic diagram was positioned (Figure 1a) by virtue of previous data.[24] The binary system (ice – $Mn(NO_3)_2$) exhibits several hydrates (i.e., $Mn(NO_3)_2 \cdot nH_2O$ where n = 1, 2, 4 and 6) contingent on the mass fraction of anhydrous salt. Previous experimental and computational studies (extended universal quasichemical (UNIQUAC) model[4]) reveal an eutectic point at a 40% mass fraction of salt and establish the eutectic depth (ΔT), a metric that sheds light on the diversity and magnitude of intermolecular interactions.[28] In Figure 1a, ΔT separates the line of ideality from the eutectic temperature T_e. The solutions are located on either side of the eutectic point in regions poor (solutions S1 and S2) and rich (solutions S3 and S4) in salt. The stable solution S3 is practically identical to the eutectic composition with an eutectic depth reaching 53 °C, in line with previous reports.[18b,24]

Table 1. Composition of the $Mn(NO_3)_2$ aqueous solutions in mass ratio, *w* (%); molal concentration in salt, $\mathcal{M}$ (mol kg^{-1}) and Mn^{2+} molar concentration *C* (mol L^{-1}).

Solution	S1	S2	S3	S4
w (%)	0.92	1.84	0.42	0.48
$\mathcal{M}$ (mol kg^{-1})	1.02	2.05	4.1	5.13
C (mol L^{-1})	0.96	1.84	3.43	4.18

The thermograms of solutions S2 and S3 are presented in Figure 1b. The temperatures (T_m and T_e) recorded on the two thermograms (Figures 1b) for each solution agree with the coordinates of the eutectic diagrams (Figure 1a). The onset temperature of fusion of both mixtures is ca. $T_e = -36$ °C and the end of their fusion depends on the composition. The melting point of the S2 solution reaches −14 °C and for S3 −29 °C consistent with the literature.[24] Figures 1c and 1d show the variation of the density (ρ) of all solutions as a function of temperature and its modelled results following the below equation 1:

$$\ln(\rho) = \beta - \alpha T(K) \quad (1)$$

The outcome of the modelling yields the thermal expansion coefficient α, a useful parameter for energy storage applications as it reflects the structuring ability of the solutions under thermal agitation and quantifies the volume increase that the system undergoes in a given temperature range.

The density values of the S2 and S3 solutions are comparable to those in the literature at room temperature and a concentration of 2 mol kg^{-1}.[24] On the other hand, they appear noticeably larger (by 23%) than their alkaline nitrate salt counterparts such as sodium nitrate ($NaNO_3$) which hold a density of 1.182 g cm^{-3} for a concentration of 4 mol kg^{-1} at 25 °C.[29] The S1–S4 solutions appear dense and structured as the salt concentration increases, which is logical for divalent salts.[30] All exhibit a monotonic variation of density with temperature (Figure 1c), with a thermal expansion coefficient of ca. $-3.9 \pm 0.2\ 10^{-4}$ K^{-1}, lower than the one for water (i.e., $-6.70\ 10^{-4}$ K^{-1}) and pure hexahydrate salt ($-5.5 \pm 0.2\ 10^{-4}$ K^{-1}, Figure 1a).

The ionic conductivity (σ) of the S1–S4 solutions as a function of concentration and temperature (−20 to 80 °C) is presented in Figures 2a and 2b, highlighting two essential criteria for energy storage electrolytes, namely a wide temperature window and ionic diffusion. In Figure 2a, the conductivity at room temperature reaches 120 mS cm^{-1} at a $\mathcal{M}_{max}$ of 4 mol kg^{-1}. In this state (i.e., eutectic ratio) the interactions between the ions are the weakest. The water molecule acts as a dipole and separates the Mn^{2+} hydrate and NO_3^- ions, which propagates their self-diffusion. When compared to the max-

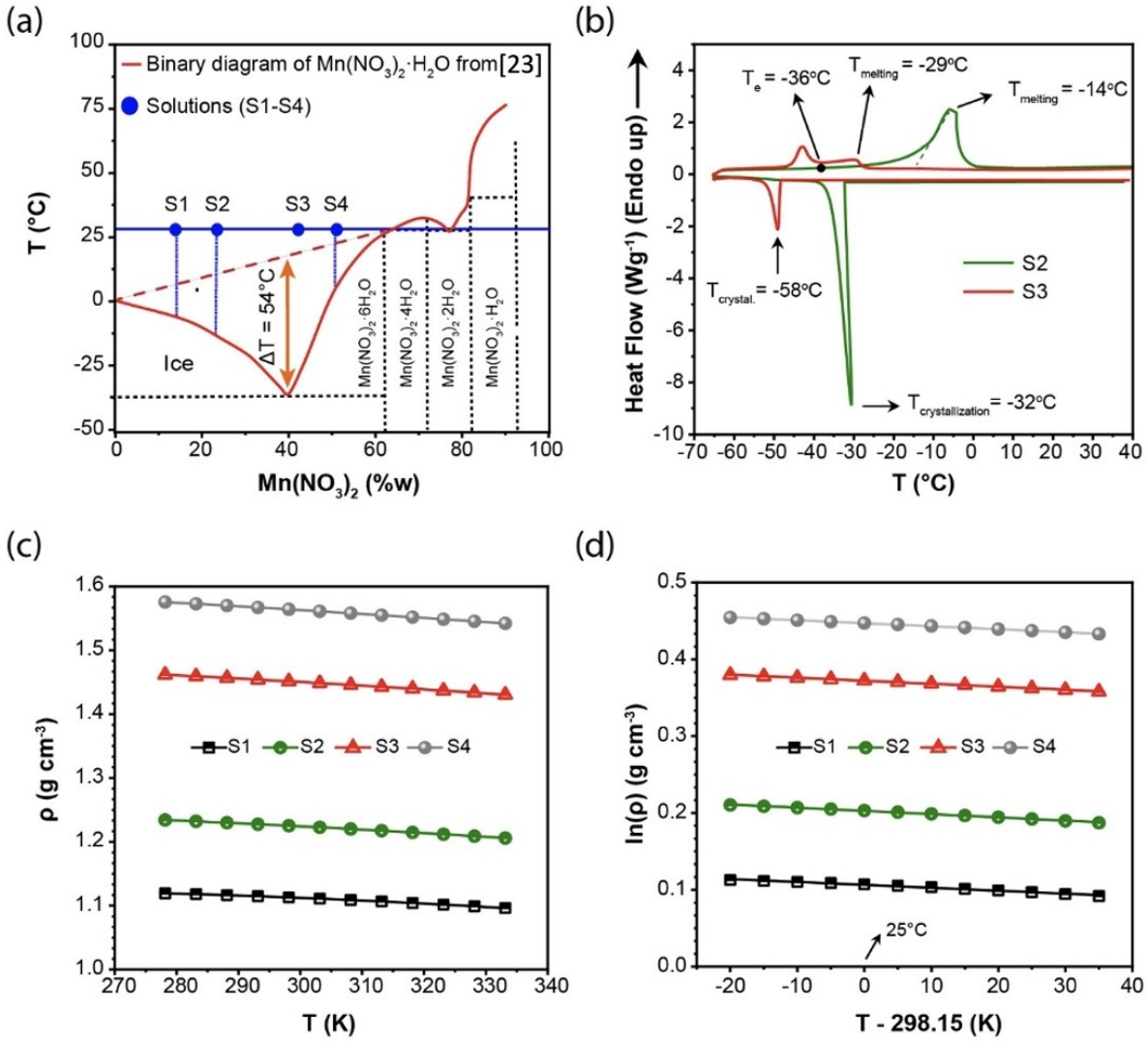

Figure 1. (a) Eutectic diagram of the aqueous $Mg(NO_3)_2$ solution constructed with the aid of reference,[24] incorporating the position of the four solutions used in this study (S1–S4) (b) Thermograms of S2 and S3 solutions. (c) Evolution of density, ρ as a function of temperature for the S1–S4 solutions (d) Modelling of density, ρ versus temperature for the same solutions.

imum conductivity (σ_{max}) of a solution comprising nitrate monovalent salts ($NaNO_3$), σ_{max} is slightly larger (i.e., 160 mS cm^{-1} at C_{max} of 4 mol L^{-1} and 25 °C[31]). This difference derives from the better diffusion of small cations rendering them more mobile in water.[32] Taking into account the size, charge density and polarizability of Mn^{2+} with other cations such as Li^+, Na^+ and Mg^{2+} (Table 2), the former can be classified as one of the relatively "strongest" hard acids in the HSAB theory following the order $Mn^{2+} < Mg^{2+} < Na^+ < Li^+$.

The classification of cations as "hard acids" in the HSAB theory depends on their polarizability, size, and charge density. The environment is equally important, including the solvent (here water, which is a hard base), the counter anion (i.e., NO_3^- which is a hard base) and the interface with the substrate, for instance, a negatively polarized electrode for supercapacitor application as discussed below. The delocalization of the negative charge leads to a greater polarizability of NO_3^-, and therefore makes it possible to soften the base character of this anion according to the HSAB theory. The Mn^{2+} cations (hard acid) preferentially associate with H_2O (a harder base than NO_3^-)[33]) and are easily separated from the NO_3^- anions in the solution. Therefore, the $Mn(H_2O)_n$ complex in hydrated salts establishes HBD-HBA (hydrogen bond acceptor) interactions with water molecules (ice) to promote the formation of an

Table 2. Ionic radii, charge density, polarizability, acidity in HSAB theory for Li^+, Na^+, Mg^{2+}, NO_3^- and Mn^{2+} and NO_3^-. The values of the first four cations are taken from.[34,35]

Properties	Li^+	Na^+	Mg^{2+}	Mn^{2+}	NO_3^-
Ionic radius (pm)	76	102	78[a]	91[b]	178
Charge density (C mm^{-3})	52	24	120	84	–
Polarizability (Å^3)	0.029	0.181	0.094	0.54	4.13
Hard Acidity (HSAB)	+++	++	++	+	–

[a] 4-coordinate, tetrahedral, [b] 6-coordinate, octahedral.

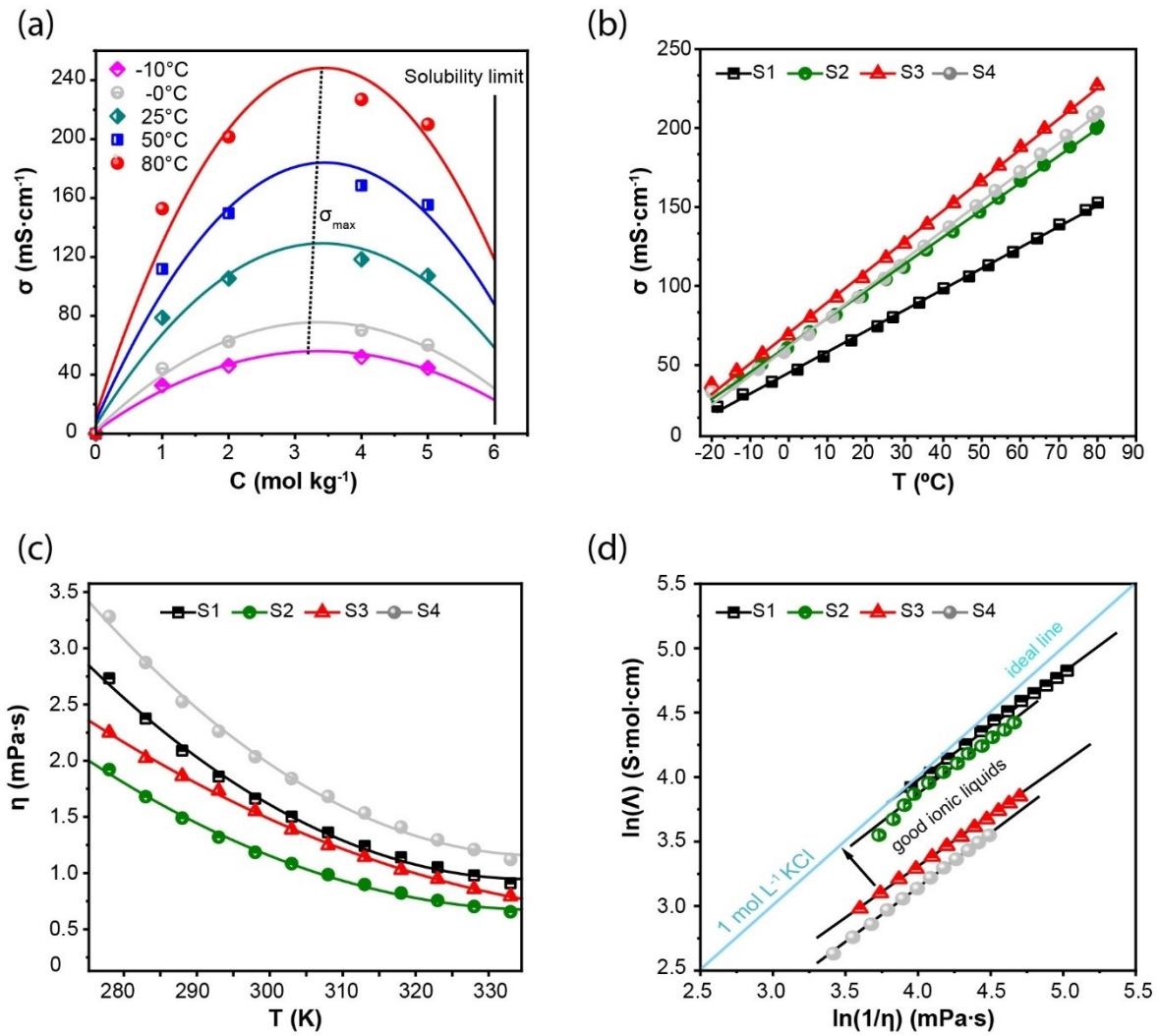

Figure 2. (a) Evolution of conductivity as a function of $Mn(NO_3)_2$ concentration. Evolution of conductivity (b) and viscosity (c) with temperature for aqueous solutions of $Mn(NO_3)_2$ (S1–S4). (d) Comparison of the ionicity of the studied solutions (S1–S4) through the Walden diagram.

eutectic mixture. The maximum interactions are expected at the eutectic composition of solution **S3**, the solution closest to the eutectic point.

The variation of the conductivity with temperature (Figure 2b) shows a monotonic increase for all examined solutions. At 80 °C, σ_{max} extends to 238 mS cm^{-1} for the S3 solution. At room temperature, the ionic conductivity hinges on 125 mS cm^{-1} in line with other aqueous electrolytes such as lithium nitrate ($LiNO_3$, 130 mS cm^{-1} at ~4 mol kg^{-1}) and sodium nitrate ($NaNO_3$, 198 mS cm^{-1} at 12 mol L^{-1}).[36] Surprisingly, $Mn(NO_3)_2$ attests to a higher conductivity than that of homologous divalent salts such as $Mg(NO_3)_2$ (e.g., 12 mS cm^{-1} at 4 mol kg^{-1})[37] where σ_{max} is located around 1 mol kg^{-1}. As expected, the residual conductivity decreases with lower temperatures and at −20 °C extends to 20 mS cm^{-1}, consistent with aqueous concentrated (7 mol kg^{-1}) zinc chloride solutions, viz. 20 and 2 mS cm^{-1} at −20 and −60 °C, respectively.[38] Therefore, hydrated salts of transition metals appear promising for integration in low-temperature storage systems.

Figure 2c describes the evolution of the dynamic viscosity (η) between 5 and 60 °C for the examined solutions. At 25 °C, the achieved viscosity complies with the literature for the stoichiometric solution $Mn(NO_3)_2 \cdot 6H_2O$ at 6.5 mol kg^{-1}, i.e., $\eta =$ 7.7 mPa·s.[18b] A 2.5-fold increase in the manganese concentration results in the doubling of the dynamic viscosity at room temperature (0.75→1.5 mPa·s). The combination of the fluidity $\left(\frac{1}{\eta}\right)$ and molar conductivity (Λ) by means of the Walden graph (Figure 2d) makes it possible to compare the ionicity of the solutions, normalized and positioned according to the ideal line of a potassium chloride aqueous solution (KCl_{aq}). A superposition of solution S1 with the line of ideality is evident in Figure 2d, while the rest move away as the concentration increases (S2→S3 solutions). The slope of the line (represented by $\Lambda = f\left(\frac{1}{\eta}\right)$) is close to unity, signifying a total dissociation of the salt,[39] meagrely affected by temperature. The above finding

is consistent with the reported favourable dissociation of manganese hexahydrate ($\Delta H_R = -5$ kJ mol^{-1}).[24]

Furthermore, we sought to model the solutions' transport properties (η, σ) as a function of temperature and extract the activation energies of the ion mobility and diffusion processes. The modelling is based on the Arrhenius and Vogel-Fulcher-Tammann (VTF) models (Equations 2&3) contingent on the deviation from the glass transition temperature of the compound. The VTF model provides a parametric correction of the temperature with T_0 representing the ideal gas transition temperature[40] and B_σ, the pseudo-activation energy (Equation 3). For all solutions, the viscosity is described by the Arrhenius relationship (Figure 3a), while the conductivity exhibits a non-Arrhenius behaviour and has been modelled by the VTF equation (Figure 3b). The activation energies (E_a^η and B_σ) are presented in Table 3.

$$\eta = \eta_0 \exp\left[\frac{-E_a^\eta}{RT}\right] \quad (2)$$

Table 3. Arrhenius and VTF fitting parameters of the viscosity and conductivity plots of Figure 2. R^2 describes the goodness of fit.

Solution	Conductivity			Viscosity	
	T_0 (K)	B_σ (kJ mol^{-1}) ±0.05	R^2	E_a^η (kJ mol^{-1}) ±0.05	R^2
S1	165 °C	2.38	0.999	14.96	0.998
S2	163 °C	2.48	0.999	13.29	0.997
S3	158 °C	2.50	0.999	15.29	0.997
S4	159 °C	2.63	0.999	14.90	0.997

$$\sigma = \sigma_0 \exp\left[\frac{B_\sigma}{T - T_0}\right] \quad (3)$$

The T_0 values stemming from the VTF model are similar for all solutions (Table 3) and close to the experimental values of glass transitions of water ice.[41] The activation pseudo-energies increase slightly at higher salt concentrations (B_σ ~2.5 kJ mol^{-1}, Table 3). When compared with energies of solutions comprising

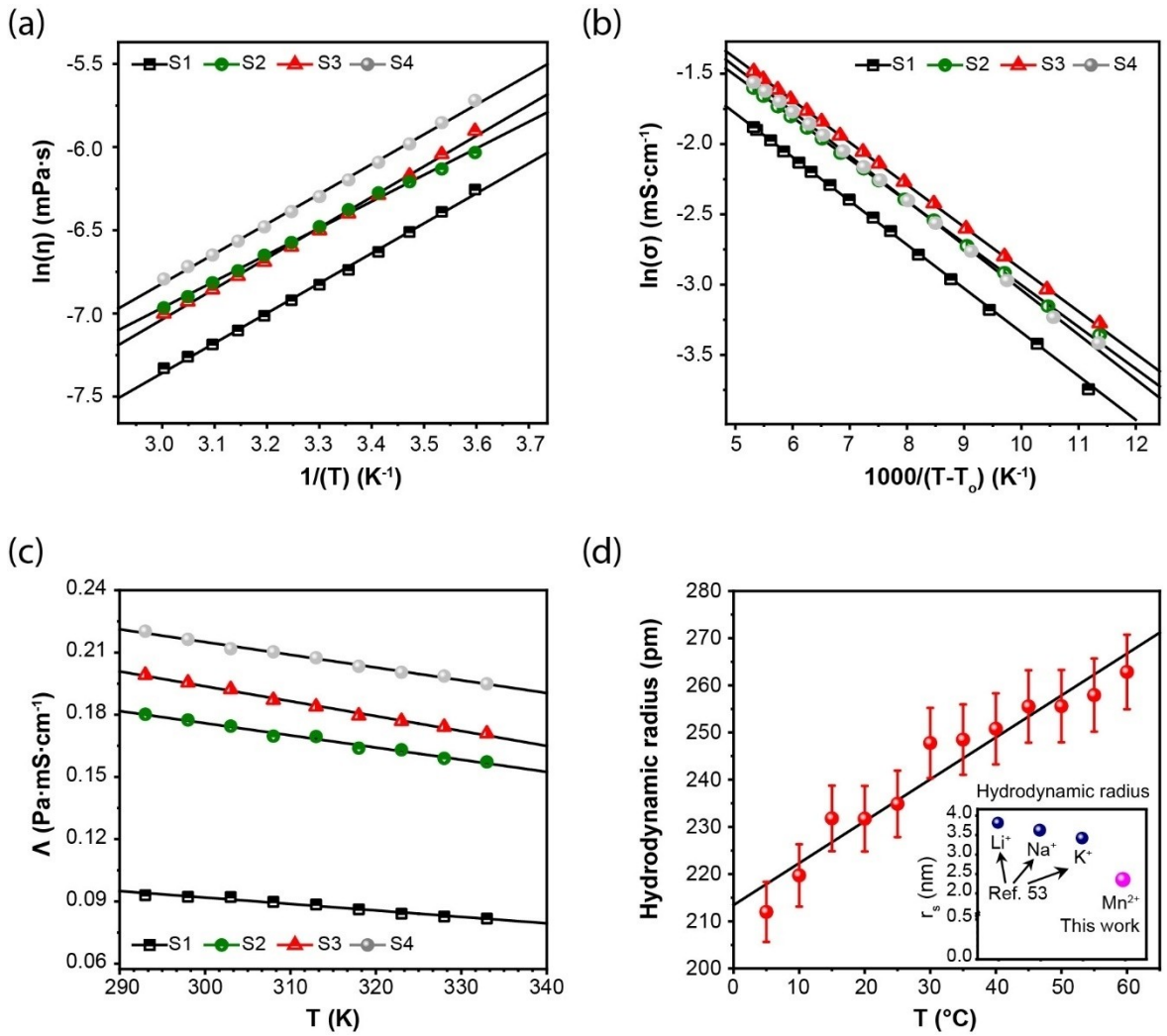

Figure 3. Fitting of the (a) viscosities and (b) conductivities of the solutions under study (S1–S4) by the Arrhenius and VTF models, respectively. (c) Walden product ($\Lambda = \sigma \times \eta$) as a function of temperature for the solutions S1–S4. (d) Effective hydrodynamic radius (r_s) of hydrated Mn^{2+} cations, derived from the Jones-Dole-Kaminsky (JDK) equation as a function of temperature. For comparison purposes, the Li^+, Na^+ and K^+ radii are taken from.[42]

alkaline salts in water[42] (i.e., B_σ ~10 to 15 kJ mol^{-1} depending on concentration), they are lower. This difference explains the dissimilarity in conductivity observed previously (Figure 2).

For the viscosity, the activation energies (E_a^η) linger close to 14 kJ mol^{-1} with no notable difference between them (Table 3) and are conforming to other aqueous solution analogues.[43] The highest activation energy is obtained by solution **S3**, probably due to the strong interaction between H_2O and Mn^{2+} in this composition, where the eutectic depth is maximum ($\Delta T = 53\,^\circ C$, Figure 1a). This is not surprising since most of the energy of the viscous flow is related to the hydrogen bonds of water. The ion mobility (σ) and viscous flux (η) are decorrelated from temperature since the Walden product, Λ, is not constant with temperature (Figure 3c). The falling Walden plots attest that the rate of decrease of the viscosity is faster than the rate of increase of the conductivity. Similar behaviour has been reported in concentrated hydrated salts, described as fragile compounds in Angel's concept[44] where their ionic mobility is conserved at low temperatures, in turn leading to the variation of Λ. It should be noted that Λ is higher at low temperatures (290→300 K) and for the most concentrated solution (S4). This can be understood by the dissociating action of water, which has strong interactions with the cation, especially close to the eutectic point (Figure 1a).

The salt concentration plays a key role in the intermolecular interactions, including the van der Waals interactions and the hydrogen bonding in water. The Jones-Dole-Kaminsky extended equation (Equation 4) enables the adjustment of the ratio η_r at high concentrations. η_r equals to $\frac{\eta}{\eta_0}$, where η and η_0 describe the viscosities of the solution and pure water, respectively.[44] *A*, *B* and *D* are the adjustment parameters of this equation. The solute-solvent short-distance interactions (*B*) are derived from Equation 5.[45] From this fitting parameter, the effective solute radius r_s^B can be computed through Equation 6 using the Einstein theory on the model of solid spheres in solution and the solvent crown around solvated ions.[46]

$$\eta_r = 1 + A\sqrt{C} + BC + DC^2 \quad (4)$$

$$\eta_r - 1 = f(C) \quad (5)$$

$$B = 2.5\left(\frac{4}{3}\pi {r_s}^3 N_A\right) \quad (6)$$

An estimation of the hydrodynamic radius r_s is given in Figure 3d where the dimensions of the solvation radius conform to a sphere with a single crown of solvent at different temperatures. When compared to other hydrated alkali cations (Li, Na, K) at 25 °C, (inset of Figure 3d) the manganese cation has the smallest radius (235 pm), about two times that of Li(H_2O). Yet, this result is counterintuitive when the ionic radii of these elements are taken into consideration. From Table 2, $r(Li^+) < r(Mg^{2+}) < r\ (Mn^{2+}) < r\ (Na^+)$. Figure 3d points out that at elevated temperatures (>40 °C) the Mn^{2+} radius (260 pm) remains 1.4 times smaller than that of Li(H_2O) (380 pm).[42] This appears logical since for Mn^{2+} the hydration is favourable (hexahydrate), particularly around the eutectic point where the H_2O-Mn^{2+} interactions are optimal. These observations are in agreement with previous studies[19,47] in aqueous $Mn(NO_3)_2$ solutions up to ~6 mol L^{-1}, where no indication of nitrate complex formation was observed and also corroborated by Figure S1 where the bands of the fully hydrated species (for solution S3), $NO_3^-{}_{aq}$ and $[Mn\text{-}(OH_2)_6]^{2+}{}_{(aq)}$ are characterized and assigned by Raman spectroscopy, UV-Vis spectroscopy and FT-IR.

Overall, taking into account the main requirements for low-temperature aqueous electrolytes)[42] *viz.*, low activation energy, small hydration radius, large supercooling ability, and mediator redox ability, the concentrated manganese hydrate solution S3 fulfils these characteristics and thus is used as an electrolyte in a symmetric electrochemical double-layer supercapacitor.

Electrochemical characterisation

The working principle of an electrochemical double-layer supercapacitor[48] is based on the physical adsorption of high specific surface area electrodes (in this case activated carbon with a specific surface area of 2270 cm^2). When charging, the electrode surface accumulates charge and attracts diffused anions and cations from the electrolyte to adsorb on the electrode surface in a directional arrangement, which forms a double electric layer structure. During discharge, the voltage across the electrodes decreases and the number of ions stored on the electrodes decreases.

The adsorption/desorption of the manganese cations (Mn^{2+}) at the polarized AC surface in all the investigated solutions is corroborated by rectangular cyclic voltammetry plots in Figure 4a. For the S3 solution, a typical scan rate dependence study indicates that lower scan rates (i.e., lower normalized current densities) yield higher specific capacitance values (e.g., >200 F g^{-1}, Figure 3b) as there is enough time for the Mn^{2+} ions to penetrate the pores leading to high charges. The permeation of these ions is quite efficient, since for an eight-fold increase in the scan rate (5→40 mV s^{-1}) the difference in the specific capacitance is less than 12%. It should be noted that alike behaviour is evidenced for the other solutions too (Figure S2).

The electrochemical window of the S3 solution lies between 1.0 and 1.6 V (Figure 3c), where a fill factor[49] of 66% is achieved for the most extended voltage, at 25 °C. Interestingly, when the temperature drops to −20 °C, the electrochemical window is not greatly affected. On the contrary, an extension is observed while the SC holds the same fill factor (for the same scan rate). The cycleability of the SC at both temperatures is given in Figure 5 and at different current densities in Figure S3. In ambient conditions (i.e., cell voltage of 1.4 V and normalized current density of 1.9 A g^{-1}) for 2000 cycles (Figure 5a) the SC generates a stable discharge specific capacitance of ~170 F g^{-1} (with 92% capacitance retention). The optimal concentration of ions in the aqueous hydrate $Mn(NO_3)_2$ solution led to the double-layer of ions at the interface between the activated carbon and electrolyte becoming more compact, in turn boosting the charge stored per unit area, namely 170 F g^{-1}, in

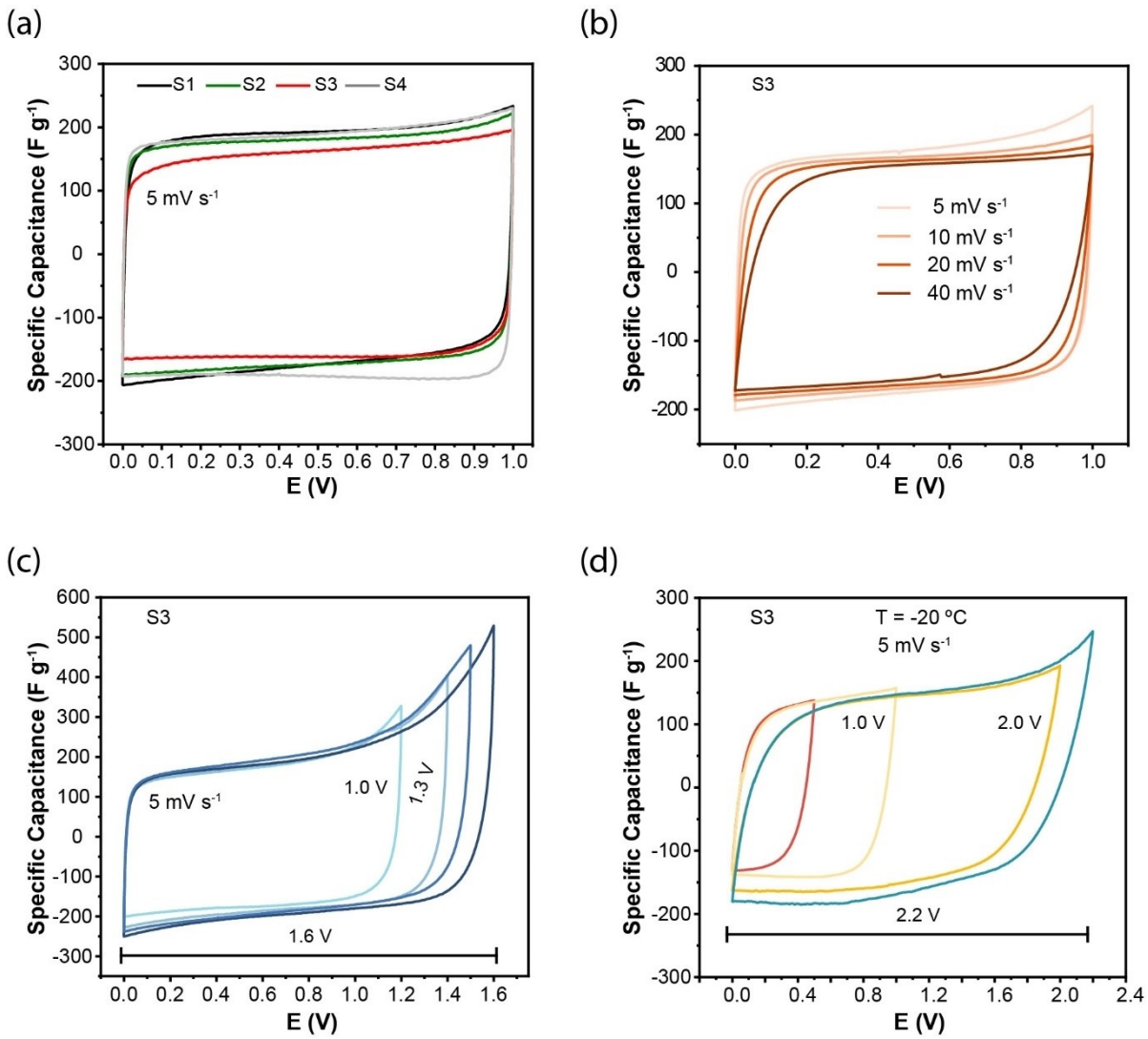

Figure 4. (a) Cyclic voltammetry profiles of two electrode symmetric SCs in deep eutectic $Mn(NO_3)_2$-H_2O solutions (S1–S4) at 5 mV s^{-1}. (b) Cyclic voltammetry profiles of the SC at different scan rates in the presence of the S3 solution. Cyclic voltammetry profiles of the SC at different cell voltages with S3 solution as an electrolyte at (c) 25 °C and (d) −20 °C.

line with other studies (Table 4). What's more, at −20 °C, the specific capacitance lays to ~120 F g^{-1} for the same number of cycles and normalized current density. Here, the lower capacitance stems from the high equivalent series resistance (i.e., ohmic drop) observed at this temperature, which reaches 300 ohms (compared to 47 ohms for the cell run at 25 °C).

Table 4. Specific capacitance of this work against other concentrated aqueous electrolytes. The normalized current density and electrodes (anode & cathode) are also provided. EC: ethylene carbonate; EG: ethylene glycol; FMD: formamide; $NaSO_4$: sodium sulfate; KI: potassium iodide; LiTFSI: lithium bis(trifluoromethanesulfonyl)imide; $NaClO_4$: sodium perchlorate; NaFTFSI: sodium (fluorosulfonyl) (trifluoromethanesulfonyl) imide, NaTFSICN: sodium cyano-trifluoromethanesulfonyl imide; NaFSI: sodium bis(fluorosulfonyl)imide.

Electrode	Electrolyte	Current Density (A g^{-1})	Specific Capacitance (F g^{-1})	Reference
Wax gourd-based porous carbon	0.5 mol L^{-1} Na_2SO_4	1	167	[51]
Carbon nanorods	21 mol L^{-1} LiTFSI	1	44	[52]
Activated Carbon	8 mol L^{-1} NaTFSI	1	150	[53]
YP-50F active carbon electrode	17 mol L^{-1} $NaClO_4$	1	33	[54]
Activated Carbon	Deep eutectic (NaFSI/FMD)	0.25	120	[55]
Activated Carbon	Deep eutectic (NaFTFSI/EC)	0.5	150	[56]
Activated Carbon	Deep eutectic KI/EG	14	217	[57]
Activated Carbon	Deep eutectic hydrate $Mn(NO_3)_2$	1.9	~160–170	[this work]

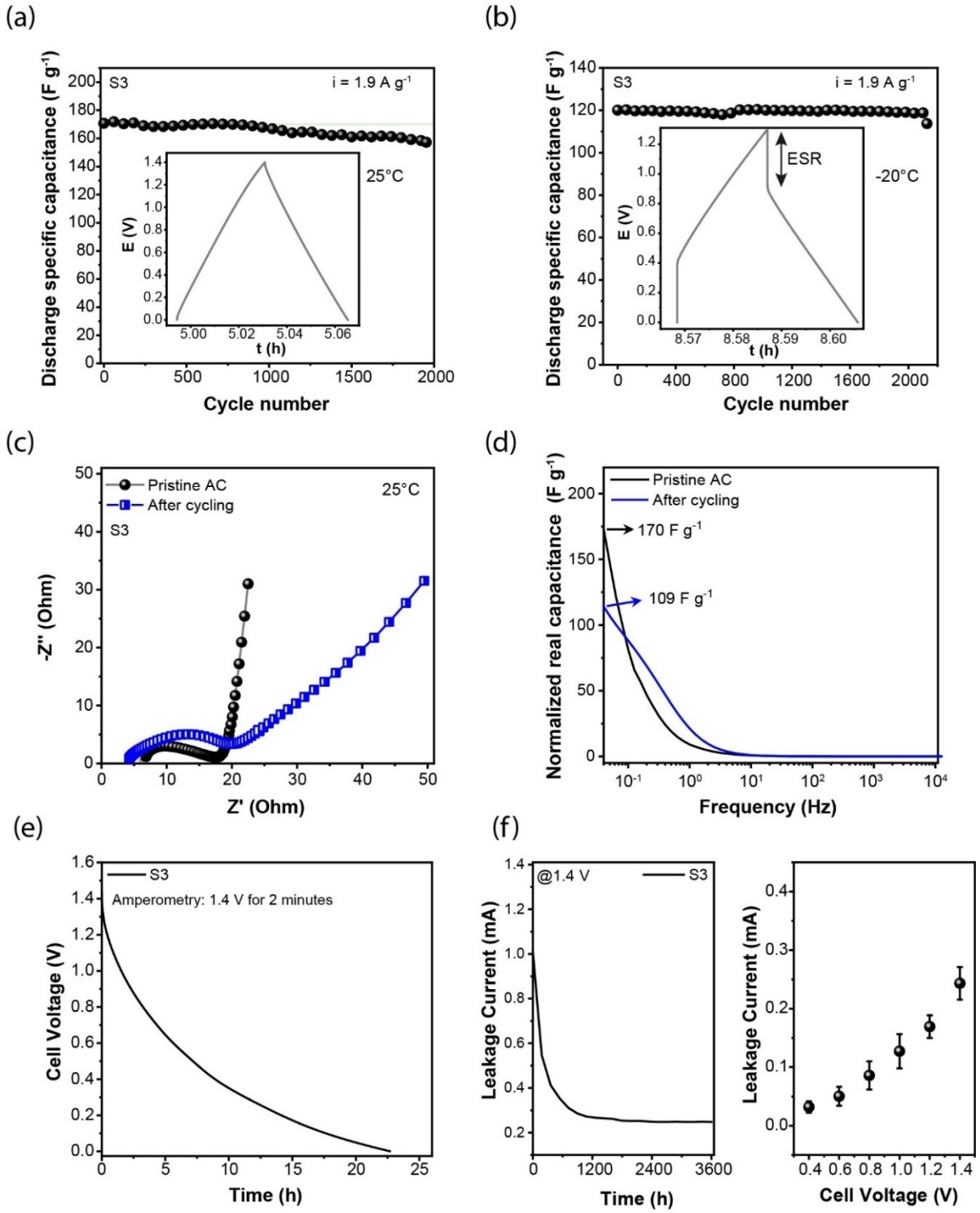

Figure 5. (a–b) Discharge specific capacitance as a function of cycle number of the SC under 1.9 A g^{-1} at (a) 25 °C and (b) −20 °C for the deep eutectic hydrate $Mn(NO_3)_2$ solution **S3**. (c) Nyquist plot of the SC before and after cycling at 25 °C. (d) Normalized real specific capacitance as a function of frequency at 25 °C. (e) Self-discharge curve of the SC under open-circuit condition for 23 h after being charged at 1.4 V for 2 minutes. (f) Leakage current at 1.4 V over 1 h (left) and leakage current at different cell voltages (right). Triplicate experiments were performed for each cell voltage.

The Nyquist plots before and after cycling at ambient conditions (Figure 5c) are quite similar, especially in the high and medium frequency regions (0.1 MHz→15 Hz). The semi-circle in the middle-frequency region describes the interfacial resistance between the electrode interface and electrolyte and is dependent on the electrolyte solution. With cycling this resistance increases (11→17 Ohm), leading to higher leakage resistance, in turn affecting the specific capacitance (depicted as normalized real specific capacitance in Figure 5d). Besides, there is a clear shift of the onset frequency towards the lower

frequency region at the same bias voltage (here the open circuit potential) indicating slower dynamics for the SC after cycling (Figure 5d). This could explain the dissimilarity in the low-frequency region of the Nyquist plot (Figure 5c, a more inclined curve signifies a deviation from the double-layer capacity). The Raman spectra of the cycled activated carbon electrode however, showed a marginal increase in the defect level (i.e., I_D/I_G ratio) indicating modest electrode resistance, stable particle-to-particle conductivity[50] and the formation of a greater number and/or size of sp^2 clusters (Figure S4).

The self-discharge curve of the SC under open-circuit conditions for 23 h after being charged at 1.4 V for 2 minutes is presented in Figure 5e. The open circuit of the SC reached 0.05 V after 23 h, with a 56 mV per hour decrease. What's more, the leakage current was recorded during a 1 h potentiostatic holding. The current is decreasing over time and given enough time, it reaches a steady-state value (i.e., 0.487 mA, Figure 5f). An almost linear increase in the leakage current is noticed upon the application of high cell voltage (1.0→1.4 V), still, the leakage current is significantly lower (×10) than the charging current (1.9 A g^{-1}→unnormalized 8.74 mA). An effective and efficient charge/discharge of an SC requires that the amount of charge stored during the charging process should be at least 10 times higher than the charge that dissipates as a consequence of leakage.[58]

Conclusion

Aqueous electrolytes are commonly used in energy storage devices because they offer several advantages over organic electrolytes, such as lower cost, higher safety, and environmental friendliness. In this context, this study discusses the value of an easy-to-produce, widely available and inexpensive concentrated manganese nitrate electrolyte, with intriguing DES features.

First, the thermograms confirmed that the thermal coordinates (T_e and T_m) of the binary mixtures agreed with the eutectic diagram. Second, the stable hydrate manganese hexahydrate ($Mn(NO_3)_2 \cdot 6H_2O$) having a weight composition of 42% (solution S3) is almost identical to the eutectic composition with an eutectic distance (ΔT) of 53 °C. Thirdly, the density values suggest compact and structured solutions as the salt concentration increases, yielding thermal expansion coefficients of 3.9×10^{-4} K^{-1}, lower than the ones for water and pure hexahydrate salt. An explanation for the behaviour of the electrolytes' transport properties (i.e., high σ) lies in considering the Mn^{2+} cations as "hard acids", following the HSAB theory. What's more, the modelling of σ and η against temperature and concentration (i.e., Walden, Arrhenius or VTF, Jones-Dole-Kaminsky models) signifies a total dissociation of the salt, with the smallest activation energy values for conductivity (~ 2.45 kJ mol^{-1}) meagerly affected by temperature and five times lower than homologues aqueous solutions comprising alkaline salts.

These "unconventional" DESs comply with the requirements of electrolytes for energy storage applications. Hence, upon the realization of two-electrode symmetric supercapacitors, the reversibility of Mn^{2+} adsorption/desorption (rectangularity of the cyclic voltammetry and 93% specific capacitance retention) and the stability of the examined electrolytes within the applied potential limits (that can extend up to 1.6 V) were validated through 2000 consecutive galvanostatic charge-discharge cycles at 25 and −20 °C, showing applicability in different temperature environments.

In conclusion, in pursuit of alternative electrolytes (to traditional organic solvents) for energy storage applications, DESs show promising potential due to their high conductivity, wide electrochemical stability window, and environmental sustainability. As demonstrated in this study, they can be tailored to have specific properties by adjusting the composition of the solvent mixture, allowing for customization of their properties for specific (rapid) energy storage applications and more.

Experimental section

Preparation and physicochemical characterization of the electrolytes

A known quantity of manganese nitrate anhydrous salt ($Mn(NO_3)_2$, ACS reagent, 99%, Sigma Aldrich) is added by weighing 5 g of deionized water so that the mixture is homogeneous. All prepared solutions are liquid and remain liquid at 25 °C. The concentrations (in mol kg^{-1}) and the mass percentages of the prepared solutions are given in Table 1. The water content of the manganese nitrate was determined by Karl-Fischer titration (Mettler Toledo DL32 Karl Fischer coulometer using the Hydranal™-Coulomat E, Riedel-de Haen as analyte). The distilled water used for the formation of all solutions was passed through a reverse osmosis system and further treated with a Milli-Q plus 185 water purification equipment. The prepared solutions are termed S1, S2, S3, and S4 in the rest of the manuscript (Table 1).

Differential scanning calorimetry (DSC) was performed with a PerkinElmer DSC 4000 calorimeter. The samples were initially cooled to −23 °C, followed by a five-minute isothermal plateau at this temperature, and then heated up to 81 °C at a rate of 5 °C min^{-1}. The dynamic viscosity and density of the electrolytes were measured using an Anton Parr densitometer comprising a digital vibrating tube densitometer and a rolling-ball viscometer (Lovis 2000 M/ME, Anton Parr, France). The densitometer and viscometer were pre-calibrated with ultra-pure water. The ionic conductivity measurements were performed by a BioLogic® multi-channel conductometer based on a frequency response analyzer (MCM 10) that was connected to a Peltier-based temperature control functioning between −20 and 75 °C. The conductometer was pre-calibrated with a standard potassium chloride (KCl, Sigma-Aldrich) solution.

The Raman spectra of the S3 solution and the activated carbon electrodes were obtained by an inVia™ confocal Raman microscope (Renishaw) under a 532 nm laser excitation and a 20× magnification lens. The deconvolution of the D and G bands of the activated carbon was done by Lorentzian fitting. The S3 solution was placed in a quartz glass cuvette (Ossila, JGS3 UV) and monitored by optical spectroscopy (PerkinElmer, Lambda 750S). The **S3** solution was further characterized using Fourier transform infrared spectroscopy (FT-IR, Shimadzu IRAffinity-1S). The FT-IR, UV-Vis and Raman measurements were performed in air.

Supercapacitor assembly

Activated carbon (AC), coated on aluminium provided kindly from Blue Solution©, (France) and used as positive and negative electrodes of the supercapacitor (SC). The physical and textural parameters of the AC have been described in a previous report.[59] The AC electrodes had a diameter of 1 cm (geometric surface area of 0.785 cm^2). The separator (Whatman filter paper, GF/C, $\phi = 12$ mm) and electrodes were dried in a Buchi oven at 80 °C for 12 h to remove residual water. An electrolyte volume of 150 µL was used for the SCs. Galvanostatic charge-discharge (GCD), cyclic voltammetry (CV), potentiostatic electrochemical impedance spectroscopy (PEIS), leakage current and self-discharge measurements were performed by a Biologic potentiostat (Biologic, France) using a two-electrode Swagelock® cell. CV plots were performed relative to the set electrochemical window at designated scan rates and normalized with respect to the active mass of the activated carbon (i.e., ~4.6 mg). The specific capacitance (F g^{-1}) of the EDLC was determined according to equations reported in previous studies.[60]

Acknowledgements

The authors thank "La Région Centre Val de Loire" for financial support.

Conflict of Interests

The authors declare no conflict of interest.

Data Availability Statement

The data that support the findings of this study are available from the corresponding author upon reasonable request.

Keywords: Deep eutectic solvent · manganese (II) nitrate hydrate · activated carbon · supercapacitor

[1] X. Zhang, J. Chen, Z. Xu, Q. Dong, H. Ao, Z. Hou, Y. Qian, *Energy Storage Mater.* **2022**, *46*, 147–154.
[2] D. Han, C. Cui, K. Zhang, Z. Wang, J. Gao, Y. Guo, Z. Zhang, S. Wu, L. Yin, Z. Weng, F. Kang, Q.-H. Yang, *Nat. Sustain* **2022**, *5*, 205–213.
[3] a) B. Nanda, M. Sailaja, P. Mohapatra, R. Pradhan, B. B. Nanda, *Mater. Today: Proc.* **2021**, *47*, 1234–1240; b) J. Afonso, A. Mezzetta, I. M. Marrucho, L. Guazzelli, *Green Chem.* **2023**, *25*, 59–105.
[4] Ž. Knez, E. Markočič, M. Leitgeb, M. Primožič, M. K. Hrnčič, M. Škerget, *Energy* **2014**, *77*, 235–243.
[5] a) S. Keskin, D. Kayrak-Talay, U. Akman, Ö. Hortaçsu, *J. Supercrit. Fluids* **2007**, *43*, 150–180; b) M. Anouti, in *Electrochemistry in Ionic Liquids: Volume 1: Fundamentals*, Springer Nature, **2015**, pp. 217–252.
[6] Y. J. Heintz, R. O. Lemoine, L. Sehabiague, B. I. Morsi, K. L. Jones, H. W. Pennline, Conference: 22nd Annual International Pittsburgh Coal Conference, Pittsburgh, PA, Sept. 12–15, **2005**.
[7] Y. Wang, W. H. Zhong, *ChemElectroChem* **2015**, *2*, 22–36.
[8] O. Borodin, X. Ren, J. Vatamanu, A. von Wald Cresce, J. Knap, K. Xu, *Acc. Chem. Res.* **2017**, *50*, 2886–2894.
[9] K. S. Lakshmi, B. Vedhanarayanan, T.-W. Lin, *Electrochim. Acta* **2023**, *447*, 142119.
[10] M. Mokhtar, M. Z. M. Talib, E. H. Majlan, S. M. Tasirin, W. M. F. W. Ramli, W. R. W. Daud, J. Sahari, *J. Ind. Eng. Chem.* **2015**, *32*, 1–20.
[11] a) F. Wan, J. Zhu, S. Huang, Z. Niu, *Batteries & Supercaps* **2020**, *3*, 323–330; b) T. Lv, L. Suo, *Curr. Opin. Electrochem.* **2021**, *29*, 100818; c) L. Suo, O. Borodin, T. Gao, M. Olguin, J. Ho, X. Fan, C. Luo, C. Wang, K. Xu, *Science* **2015**, *350*, 938–943.
[12] X. Tian, Q. Zhu, B. Xu, *ChemSusChem* **2021**, *14*, 2501–2515.
[13] Y. Deng, Y. Wu, K. Zhang, M. Fan, L. Wang, Y. He, L. Yan, *J. Mater. Chem. A* **2023**, *11*, 8368–8379.
[14] P. Janicka, M. Kaykhaii, J. Płotka-Wasylka, J. Gębicki, *Green Chem.* **2022**, *24*, 5035–5045.
[15] D. Yu, Z. Xue, T. Mu, *Chem. Soc. Rev.* **2021**, *50*, 8596–8638.
[16] Y. Liu, J. B. Friesen, J. B. McAlpine, D. C. Lankin, S.-N. Chen, G. F. Pauli, *J. Nat. Prod.* **2018**, *81*, 679–690.
[17] E. L. Smith, A. P. Abbott, K. S. Ryder, *Chem. Rev.* **2014**, *114*, 11060–11082.
[18] a) A. P. Abbott, C. D'Agostino, S. J. Davis, L. Gladden, M. Mantle, *Phys. Chem. Chem. Phys.* **2016**, *18*, 25528–25537; b) Y. Marcus, *ACS Sustainable Chem. Eng.* **2017**, *5*, 11780–11787.
[19] R. Caminiti, P. Cucca, T. Pintori, *Chem. Phys.* **1984**, *88*, 155–161.
[20] a) H. Ye, Y. Li, *Energy Fuels* **2021**, *35*, 7624–7636; b) S. Ponnada, M. S. Kiai, R. Krishnapriya, R. Singhal, R. K. Sharma, *Energy Fuels* **2022**, *36*, 6013–6026.
[21] C. Zhong, Y. Deng, W. Hu, J. Qiao, L. Zhang, J. Zhang, *Chem. Soc. Rev.* **2015**, *44*, 7484–7539.
[22] M. Arrad, M. Aliyeva, S. M. Vilas-Boas, M. Kaddami, H. Sippola, P. Taskinen, S. P. Pinho, *J. Solution Chem.* **2018**, *47*, 774–786.
[23] H. Danninger, C. Gierl-Mayer, M. Prokofyev, M.-C. Huemer, R. de Oro Calderon, R. Hellein, A. Müller, G. Stetina, *Powder Metall.* **2021**, *64*, 115–125.
[24] M. Arrad, M. Kaddami, J. Maous, K. Thomsen, *Fluid Phase Equilib.* **2015**, *397*, 126–130.
[25] M. C. Iliuta, K. Thomsen, P. Rasmussen, *AlChE J.* **2002**, *48*, 2664–2689.
[26] a) G. Huang, Q. Geng, B. Xing, Y. Liu, Y. Li, Q. Liu, J. Jia, L. Chen, C. Zhang, *J. Power Sources* **2020**, *449*, 227506; b) S. Bi, S. Wang, F. Yue, Z. Tie, Z. Niu, *Nat. Commun.* **2021**, *12*, 6991; c) I. Hussain, D. Mohapatra, G. Dhakal, C. Lamiel, S. G. Mohamed, M. S. Sayed, J.-J. Shim, *J. Energy Storage* **2020**, *32*, 101767.
[27] A. P. Abbott, C. D'Agostino, S. J. Davis, L. F. Gladden, M. D. Mantle, *Phys. Chem. Chem. Phys.* **2016**, *18*, 25528–25537.
[28] A. van den Bruinhorst, M. Costa Gomes, *Curr. Opin. Green Sustain. Chem.* **2022**, *37*, 100659.
[29] T. Isono, *J. Chem. Eng. Data* **1984**, *29*, 45–52.
[30] Y. Marcus, *J. Chem. Eng. Data* **2013**, *58*, 488–491.
[31] W. Wu, S. Shabhag, J. Chang, A. Rutt, J. F. Whitacre, *J. Electrochem. Soc.* **2015**, *162*, A803.
[32] a) S. Koneshan, J. C. Rasaiah, R. M. Lynden-Bell, S. H. Lee, *J. Phys. Chem. B* **1998**, *102*, 4193–4204; b) Z. Guo, T. Wang, H. Wei, Y. Long, C. Yang, D. Wang, J. Lang, K. Huang, N. Hussain, C. Song, B. Guan, B. Ge, Q. Zhang, H. Wu, *Angew. Chem. Int. Ed.* **2019**, *58*, 12569–12573.
[33] R. G. Pearson, *J. Chem. Educ.* **1968**, *45*, 581.
[34] a) V. Dimitrov, T. Komatsu, *J. Ceram. Soc. Jpn.* **1999**, *107*, 879–886; b) J. Shanker, H. P. Sharma, B. R. K. Gupta, *Solid State Commun.* **1977**, *21*, 903–905.
[35] M. Li, B. Zhuang, Y. Lu, Z.-G. Wang, L. An, *J. Phys. Chem. B.* **2017**, *121*, 6416–6424.
[36] J. Jiang, B. Liu, G. Liu, D. Qian, C. Yang, J. Li, *Electrochim. Acta* **2018**, *274*, 121–130.
[37] A. Wahab, S. Mahiuddin, G. Hefter, W. Kunz, *J. Chem. Eng. Data* **2006**, *51*, 1609–1616.
[38] Q. Zhang, Y. Ma, Y. Lu, L. Li, F. Wan, K. Zhang, J. Chen, *Nat. Commun.* **2020**, *11*, 4463.
[39] J. Chidiac, L. Timperman, M. Anouti, *J. Energy Chem.* **2022**, *65*, 352–366.
[40] S. Amara, J. Toulc'Hoat, L. Timperman, A. Biller, H. Galiano, C. Marcel, M. Ledigabel, M. Anouti, *ChemPhysChem* **2019**, *20*, 581–594.
[41] a) C. A. Angell, *Chem. Rev.* **2002**, *102*, 2627–2650; b) C. A. Angell, R. D. Bressel, J. L. Green, H. Kanno, M. Oguni, E. J. Sare, *J. Food Eng.* **1994**, *22*, 115–142.
[42] L. Jiang, D. Dong, Y.-C. Lu, *Nano Research Energy* **2022**, *1*, e9120003.
[43] P. G. Brewer, E. T. Peltzer, K. Lage, *Deep Sea Res. Part I Oceanogr. Res. Pap.* **2021**, *176*, 103592.
[44] a) Y. R. Dougassa, J. Jacquemin, L. El Ouatani, C. Tessier, M. Anouti, *J. Phys. Chem. B.* **2014**, *118*, 3973–3980; b) M. Kaminsky, *Z. Phys. Chem.* **1956**, *8*, 173–191.
[45] a) R. S. Patil, V. R. Shaikh, P. D. Patil, A. U. Borse, K. J. Patil, *J. Mol. Liq.* **2014**, *200*, 416–424; b) N. Martinus, D. Crawford, D. Sinclair, C. A. Vincent, *Electrochim. Acta* **1977**, *22*, 1183–1187.
[46] Y. Shao, K. Shigenobu, M. Watanabe, C. Zhang, *J. Phys. Chem. B* **2020**, *124*, 4774–4780.
[47] W. W. Rudolph, G. Irmer, *Dalton Trans.* **2013**, *42*, 14460–14472.

[48] S. Wustoni, G. Nikiforidis, S. Inal, Y. S. Indartono, V. Suendo, B. Yuliarto, *APL Mater.* **2022**, *10*, 061101.
[49] G. Nikiforidis, S. Wustoni, D. Ohayon, V. Druet, S. Inal, *ACS Appl. Energy Mater* **2020**, *3*, 7896–7907.
[50] O. E. Eleri, F. Huld, J. Pires, W. M. Tucho, P. Schweigart, A. M. Svensson, F. Lou, Z. Yu, *Electrochim. Acta* **2023**, *453*, 142359.
[51] D. Yu, Y. Ma, M. Chen, X. Dong, *J. Colloid Interface Sci.* **2019**, *537*, 569–578.
[52] D. Xiao, Q. Wu, X. Liu, Q. Dou, L. Liu, B. Yang, H. Yu, *ChemElectroChem* **2019**, *6*, 439–443.
[53] D. Reber, R.-S. Kühnel, C. Battaglia, *Sustain. Energy Fuels* **2017**, *1*, 2155–2161.
[54] X. Bu, L. Su, Q. Dou, S. Lei, X. Yan, *J. Mater. Chem. A* **2019**, *7*, 7541–7547.
[55] S. Amara, W. Zaidi, L. Timperman, G. Nikiforidis, M. Anouti, *J. Chem. Phys.* **2021**, *154*, 164708.
[56] J. Chidiac, G. Nikiforidis, L. Timperman, M. Anouti, *ChemPhysChem* **2022**, *23*, e202200224.
[57] L. H. Xu, D. Wu, Y. W. Zhu, X. Y. Chen, Z. J. Zhang, *J. Energy Storage* **2022**, *48*, 103955.
[58] M. Haque, Q. Li, A. D. Smith, V. Kuzmenko, P. Rudquist, P. Lundgren, P. Enoksson, *J. Power Sources* **2020**, *453*, 227897.
[59] G. Nikiforidis, M. E. Yagoubi, M. Anouti, *Electrochim. Acta* **2022**, *402*, 139529.
[60] G. Nikiforidis, S. Phadke, M. Anouti, *Adv. Mater. Interfaces* **2023**, *10*, 2202046.

Manuscript received: April 25, 2023
Revised manuscript received: May 11, 2023
Version of record online: ■■, ■■

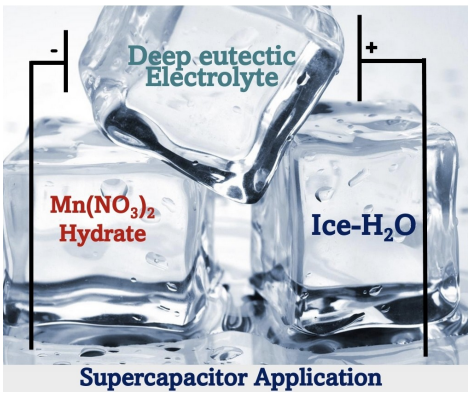

*M. Raghibi, Dr. G. Nikiforidis, Prof. M. Anouti**

1 – 12

Deep Eutectic $Mn(NO_3)_2$–H_2O Binary System as a Safe, Cost-Effective, and Efficient Electrolyte for Supercapacitor Applications

This study shows that a widely available manganese nitrate hydrate salt, when dissolved in big quantities in an aqueous medium (concentrated), behaves like a deep eutectic mixture and exhibits favourable properties for rapid energy storage application.